Journal of Digital Imaging (2023) 36:1148–1157
https://doi.org/10.1007/s10278-023-00786-0

Automatic Segmentation of Hyperreflective Foci in OCT Images Based on Lightweight DBR Network

Jin Wei[1,3] · Suqin Yu[1] · Yuchen Du[1,2] · Kun Liu[1] · Yupeng Xu[1] · Xun Xu[1]

Received: 25 October 2022 / Revised: 14 January 2023 / Accepted: 18 January 2023 / Published online: 7 February 2023

Abstract

Hyperreflective foci (HF) reflects inflammatory responses for fundus diseases such as diabetic macular edema (DME), retina vein occlusion (RVO), and central serous chorioretinopathy (CSC). Shown as high contrast and reflectivity in optical coherence tomography (OCT) images, automatic segmentation of HF in OCT images is helpful for the prognosis of fundus diseases. Previous traditional methods were time-consuming and required high computing power. Hence, we proposed a lightweight network to segment HF (with a speed of 57 ms per OCT image, at least 150 ms faster than other methods). Our framework consists of two stages: an NLM filter and patch-based split to preprocess images and a lightweight DBR neural network to segment HF automatically. Experimental results from 3000 OCT images of 300 patients (100 DME,100 RVO, and 100 CSC) revealed that our method achieved HF segmentation successfully. The DBR network had the area under curves dice similarity coefficient (DSC) of 83.65%, 76.43%, and 82.20% in segmenting HF in DME, RVO, and CSC on the test cohort respectively. Our DBR network achieves at least 5% higher DSC than previous methods. HF in DME was more easily segmented compared with the other two types. In addition, our DBR network is universally applicable to clinical practice with the ability to segment HF in a wide range of fundus diseases.

Keywords Hyperreflective foci · Optical coherence tomography · Image segmentation · Deep learning · Lightweight network

Introduction

Hyperreflective foci (HF) is defined as spot-shaped or block-shaped regions with high contrast and high reflectivity in optical coherence tomography (OCT) images [1]. Previous studies have shown that HF is mainly caused by microglia (MG) aggregation and hard exudate (HE) [2]. Besides, In addition, HF caused by MG activation appears earlier than HE and has greater clinical applications [1–3, 5–8].

HF can be considered as biomarkers for the progression, treatment response, and prognosis in retina diseases OCT, including diabetic macular edema (DME), retina vein occlusion (RVO), and central serous chorioretinopathy (CSC) [1, 3–6]. In DME, the degree of it can be assessed by the number and location of HF and the effect of the anti-VEGF treatment can be assessed by comparing the number and volume of HF [7, 9, 10]. In RVO, HF demonstrates the process of immunity to retinal immunity associated with pathogenesis, and ophthalmologists can predict the patient's best-corrected visual acuity based on the number and volume of HF [10–12]. In CSC, HF can be used to predict the time to inflammation resolution as well as the probability of recurrence [13–15]. Given the significance of HF in OCT images, it is necessary to segment them. However, manual segmentation of HF by ophthalmologists is costly, time-consuming, and susceptible to uncontrollable factors such as their work experience and status, which poses a great challenge for the application of HF [16–18].

Jin Wei and Suqin Yu contributed equally to this manuscript and thus should be considered as co-first authors.

✉ Yupeng Xu
kevinxyp@live.com

[1] Department of Ophthalmology, Shanghai General Hospital, Shanghai Jiao Tong University School of Medicine, National Clinical Research Center for Eye Diseases, Shanghai Key Laboratory of Ocular Fundus Diseases, Shanghai Engineering Center for Visual Science and Photomedicine, Shanghai Engineering Center for Precise Diagnosis and Treatment of Eye Diseases, Shanghai 200080, China

[2] Department of Automation, Shanghai Jiao Tong University, Shanghai 200240, China

[3] Shanghai Ruijin Hospital, Shanghai Jiao Tong University School of Medicine, Shanghai 200025, China

In recent years, with the development of computer science, it has made great contributions to HF segmentation algorithms, which can be divided into two main categories: traditional segmentation algorithms and deep learning–based segmentation methods. Traditional HF segmentation methods usually require manual adjustment of parameters as well as extensive a priori knowledge. Okuwobi et al. [19] proposed morphological reconstruction to estimate the HFs by extracting the extremal regions from the connected regions. However, this method lacks quantitative analysis and thus cannot be applied in clinical applications. Deep learning method has achieved great success in the medical image segmentation field. Yu et al. [20] used deep convolutional neural networks (DCNN) to automatically and accurately segment HFs of diabetic retinopathy in SD-OCT images. Since they only partially tackled the class imbalance problem, the network had the problem of misclassifying large blood vessels and low-contrast backgrounds as HF. Okuwobi et al. [19] used a 3D-Uet network for the segmentation of HF in diabetic retinopathy, which used denoised and enhanced OCT images as two-channel inputs to UNet network, and used depth-wise convolution instead of standard convolution to obtain the high-dimensional information of the OCT images. However, this method does not take into account the false positive results caused by the high-frequency noise in the NFL/GCL and IS/OS layers. The above deep learning approach for identifying HF is only applicable to segment one specific fundus disease, which means it does not have universal applicability and broad clinical merit. Moreover, the complex structure and large parameters of previous deep learning segmentation networks lead to long training times and high computing power costs, making it difficult to be applied in clinical practice [19, 20].

To address the above issue, we proposed a novel network composed of a DBR block with dilated convolution. We contributed three datasets of HF from DME, CSC, and RVO patients' OCT. On these datasets, first, we validated the effectiveness of NLM and patch-based image split methods through extensive experiments. Then, we continuously adjusted the probability thresholds to further improve the segmentation accuracy. Finally, under the condition of optimal parameter configuration, the performance of our DBR network with previous methods (UNet, UNet++, RelayNet, FCN, DeepLabv3) was evaluated.

Proposed Method

Overview

We present our HF segmentation method as shown in Fig. 1 including two steps. In the first step, we process the OCT image with NLM to remove the speckle noises. Then, we split the filtered images into patches to solve the imbalanced ratio between HFs and backgrounds. After preprocessing, we feed these patch images into the proposed DBR neural network at the second step. In our network, a coarse-to-fine architecture is designed to gradually extract the deep features hidden in the patch image with three DBR blocks of different receptive fields. Finally, we transform these features into HF segmentation results with a convolution layer of kernel size = 1 and classify each pixel with a SoftMax layer.

Dataset

The patients in this study were recruited from the Shanghai General Hospital. The study protocol was approved by the Institutional Review Board and the Ethics Committee of Shanghai General Hospital, in accordance with the principles of the Declaration of Helsinki (IRB No. 2022SQ066). The medical records of untreated patients with DME, RVO, and CSC who were followed up in the ophthalmology department of Shanghai General Hospital from January 2019 to June 2021 were retrospectively analyzed. Patients were required to have a central retinal thickness (CRT) > 300 mm and HF appearing on ≥ SD-OCT on OCT images at 10 intervals on consecutive scans. All patients with RVO and DME were free of subretinal fluid (SRF) or epiretinal membrane (ERM). Subretinal fluid was defined as well-defined, usually bell-shaped HF between the ellipsoidal region and the retinal pigment epithelium (RPE). At least 2 consecutive B-scans were required. We excluded patients with high myopia (> 6 diopters [D]), a history of uveitis, vitreous hemorrhage, glaucoma, and patients with poor image quality due to severe media clouding, poor focus, and other reasons. Only images with a quality fraction > 16 dB were selected. Informed consents were obtained from all patients.

According to the above criteria, we collect three groups of OCT images of patients with DME, RVO, and CSC (1000 images per group). In each group, we select 70% as the training set, 20% as the validation set, and 10% as the test set. Each set is independent and the HF region of an OCT image is labeled by experts. To prevent the offset in the experimental HF segmentation results due to the single dataset division, we also apply *k*-fold cross-validation [31] for computing the average of the HF segmentation metrics, where the proposed DBR neural network is trained and tested under different dataset division situations. The image size of all data sets is resized to 480 × 480 using bilinear interpolation [32] in order to maintain consistency. The clinical characteristics of the patients are listed in Table 1.

NLM Edge-Hold Denoise

The first challenge is to remove the speckle noise caused by the unstable scanning speed of the OCT machine and the

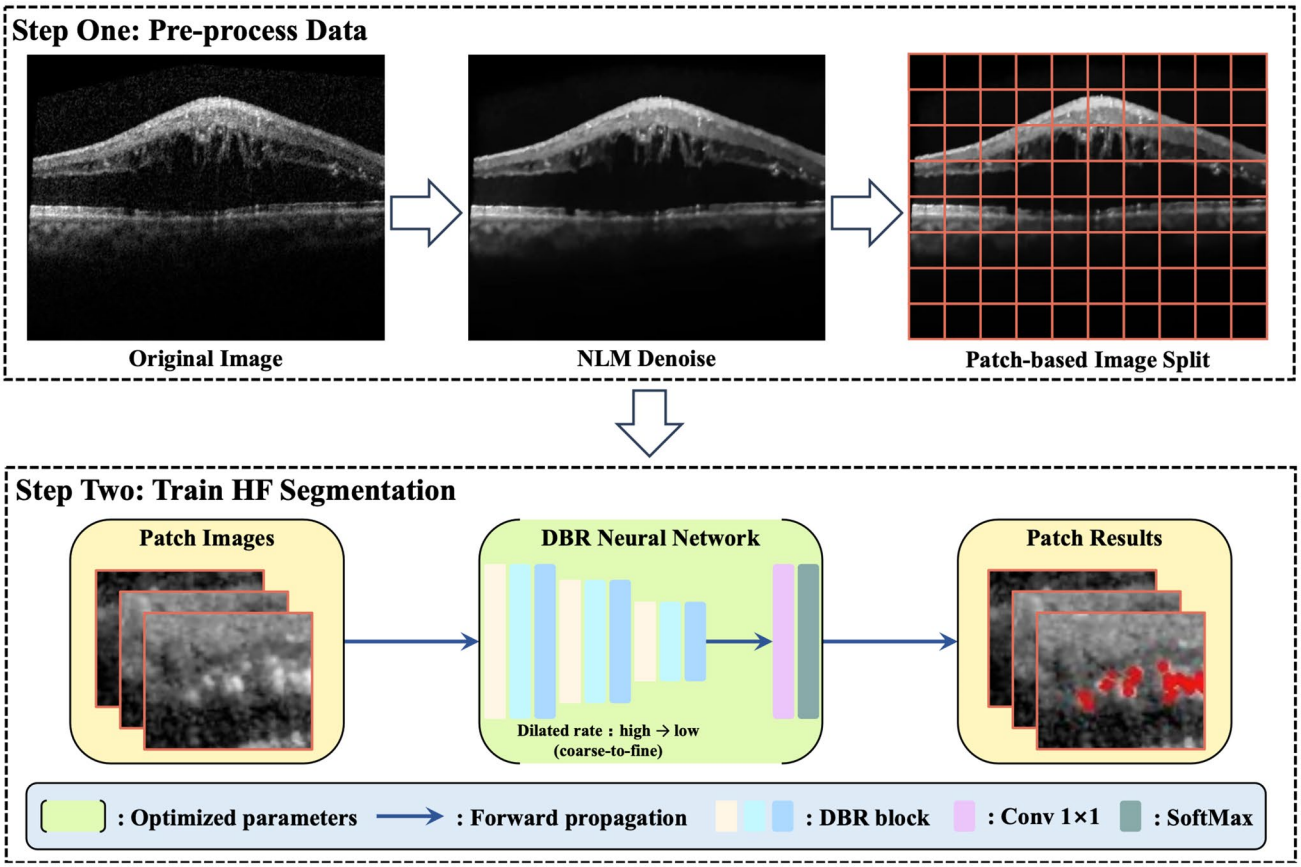

Fig. 1 Overall framework of the proposed HF segmentation method

generation of scattered particles in the eyes [21]. The speckle noise makes the boundaries of OCT images unclear leading to a low signal-to-noise ratio and bad HF segmentation results [22].

In this paper, we filter speckle noise in OCT images with the non-local means (NLM) denoise method. NLM is a global filtering algorithm, which utilizes the relationship between the whole image and local features for denoising [23]. As shown in Fig. 2, The OCT image denoised by NLM can provide more edged and detailed information for HF segmentation, while bilateral filtering only considers the neighboring information of pixels, resulting in the lack of edged representations in the bilateral filtered OCT images.

Table 1 Demographic characteristics of the data sets

Parameters	RVO	CSC	DME	P^a
Age, years	60.77 ± 8.77	51.98 ± 9.46	60.41 ± 10.65	< 0.001*
Gender, male%	43.00%	69.00%	53.00%	< 0.001*
Race	Chinese	Chinese	Chinese	/

*$P < 0.05$ was considered statistically significant

[a]The analysis of variance test was used for the comparison among three disease groups; the chi-square test was used for the comparison of the proportion of gender

Patch-Based Image Split

In Table 2, we compute the pixel occupancy of HFs against backgrounds in the three disease groups from the dataset (e.g., the average percentage of HFs is 0.5025% and the average percentage of backgrounds is 99.4975%) and observe that the percentage of pixels occupied by HFs is significantly lower than that of backgrounds. Therefore, the number of HF samples for training the network is small, making the network tend to misclassify some HF pixels as backgrounds and increase the false negative in the HF segmentation results.

To solve the above problem, we propose a patch-based image split method. We divide the images into two categories, where the patches containing HFs are used as positive samples, and the patches without HF are used as negative samples, in order to increase the proportion of HFs in positive samples. The positive and negative samples are jointly fed into the network for adversarial training to improve the ability of the network to discriminate HFs.

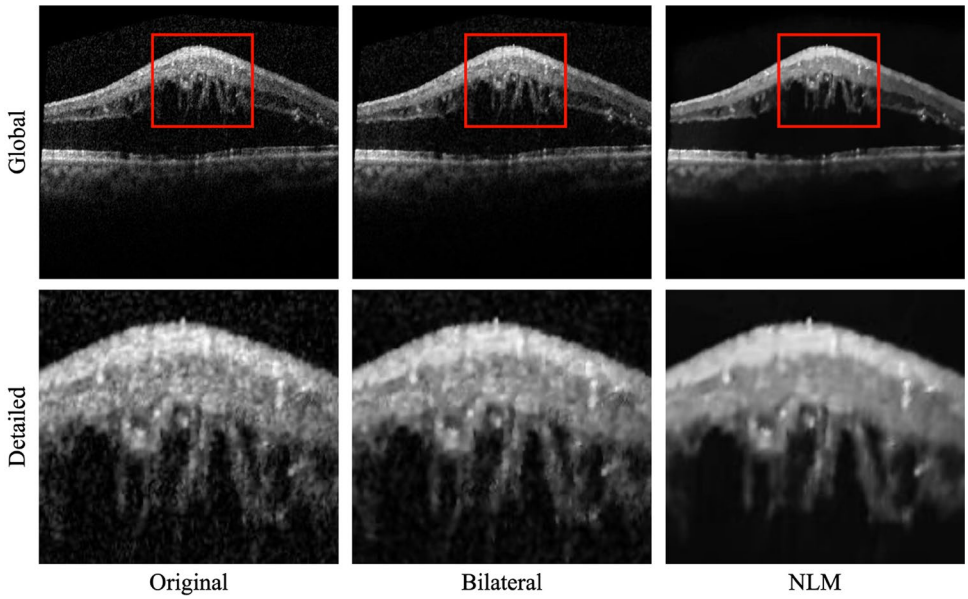

Fig. 2 Comparison of different denoise filter methods

DBR Neural Network

We propose a lightweight neural network consisting of DBR blocks. DBR block consists of dilated convolution layer, batch normalization layer, and ReLU activation function. In contrast to the convolution layer, the dilated convolution layer has wider receptive fields since the convolution kernel operates in a sparse mode [24], as shown in Fig. 3, where the orange pixels (features) are chosen as the locations to perform the convolution operation. Hence, more local features can be detected for semantic segmentation. We also apply the residual connection in the DBR block [25]. This connection strategy can avoid the gradient disappearance as the layer gets deeper and accelerate the convergence behaviors, allowing the network to reach the fine-tuning stage earlier.

The DBR block can be formulated as follows:

$$Y = X \oplus (\mathrm{DConv}\,(X, \mathrm{ReLU})) \tag{1}$$

where X denotes the input data. Y denotes the extraction result of the block layer and DConv denotes the dilated convolution (i.e., dilate rate = 4) as well as batch normalization operation. $\oplus$ denotes the residual connection.

Table 2 The proportion of HF and background pixel

Disease	Proportion of HF pixel	Proportion of background
RVO	0.5066%	99.5934%
CSC	0.5227%	99.4773%
DME	0.4783%	99.5217%
Mean (whole dataset)	0.5025%	99.4975%

The whole framework of the proposed DBR neural network is illustrated in Fig. 4. We design a hierarchical coarse-to-fine sampling architecture with DBR blocks of different dilated rates and kernel sizes. The DBR network is composed of three DBR blocks with dilated rates of 8, 4, and 1, and convolution kernel sizes of $3\times3\times64$, $3\times3\times32$, and $3\times3\times16$, respectively, which can gradually detect hidden features in small-sized images with the reduction of dilated rate and kernel. Then, we use a $1\times1\times2$ convolution layer and a SoftMax layer to map the features extracted from these DBR blocks to the maximum probability between the two categories (HFs, backgrounds) of each pixel.

Segmentation Loss Function

Our goal is to segment HFs from OCT images. With the condition of patch-based image split, we propose to apply a proportional weight factor in the loss function for improving the HF segmentation performance of the network. The formula for computing the weight coefficient is as follows:

$$w_k = \frac{\left(1/N_k\right)^2}{\left(1/N\right)^2} \tag{2}$$

where k denotes the category of HFs or backgrounds, N_k denotes the number of pixels corresponding to category k, and N denotes the number of all pixels of the images.

The segmentation loss is defined by the cross-entropy cost function and dice cost function:

$$loss_{ce} = -\sum_{n=1}^{M}\sum_{i=1}^{C} w_k y_{nk} \log\left(y_{nk}{}'\right) \tag{3}$$

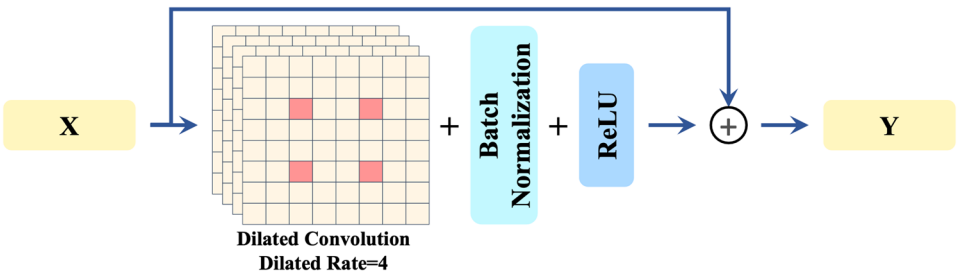

Fig. 3 The architecture of DBR block

$$loss_{dice} = 1 - \sum_{n=1}^{M}\sum_{k=1}^{C} w_k \frac{2 \cdot y_{nk} y_{nk}'}{y_{nk} + y_{nk}'} \tag{4}$$

$$loss = \lambda_1 loss_{ce} + \lambda_2 loss_{dice} \tag{5}$$

where M denotes the number of pixels in each batch, C denotes the category (background, DME or CSC or RVO), y_{nk} denotes the true value of the classification probability of the ith pixel in the nth image in every batch, $y_{nk'}$ denotes the estimated value of classification probability of the ith pixel in the nth image in a batch, w_k denotes the weight of its corresponding category, λ_1 denotes the weight factor of $loss_{ce}$, and λ_2 denotes the weight factor of $loss_{dice}$.

Experiment

Environmental Setting

The hardware environment is NVIDIA cuDNN7.5, CUDA10.0, and the configuration is RTX1050TiGPU. The neural network learns the weights of each layer by training data and verifies the performance of the model by validation data.

The setting of the Adam optimizer is shown in Table 3 below. We apply the Adam optimizer for updating the parameters of the network via the segmentation loss function mentioned in Eq. (5). We set the batch size to 32 and perform 500 epochs.

Evaluation Metrics

To quantitatively evaluate the segmentation effect of the DBR network, we employ the following metrics. The dice similarity coefficient (DSC) [26] can measure the competitive similarity between the manual HF segmentation and automatic HF segmentation by the proposed DBR neural network, which can be defined as:

$$DSC = \frac{2TP}{FP + FN + 2TP} \tag{6}$$

We also use interest over union (IOU) [38] and precision and recall to evaluate our method, which can be defined as:

$$IOU = \frac{TP}{TP + FP + FN} \tag{7}$$

$$Precision = \frac{TP}{TP + FP} \tag{8}$$

$$Recall = \frac{TP}{TP + FN} \tag{9}$$

where TP denotes the true positive, FP denotes the false positive, TN denotes the true negative, and FN denotes the false negative.

Quantitative Results of Different Patch Sizes and Probability Threshold

We gradually increase the patch size by 8 intervals in the integer range from 0 to 64 and estimate the corresponding DSC on the test dataset of three diseases, in order to search for the best patch size to split the OCT image. Figure 5 shows that the best performance can be achieved at patch size = 32. On the one hand, the larger patch size results in a lower percentage of high frequencies in the patches, making the network tend to segment all pixels into backgrounds. On the other hand, the smaller size cuts down the effective information of the patch; hence, the DBR network is harder to extract features from patches and degrade the HF segmentation quality.

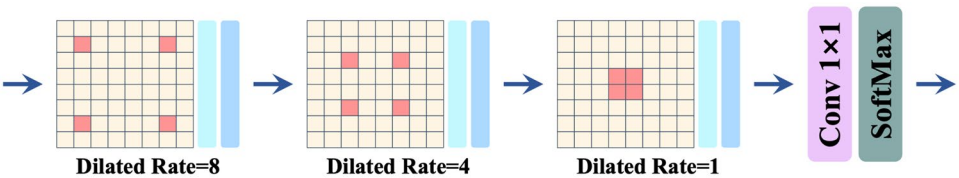

Fig. 4 The architecture of DBR segmentation network

Table 3 Hyperparameters of training

Optimizer	Adam
Learning rate	1e − 2
Learning rate decay	0.9 exponential decay per epoch
Batch size	32
Epochs	500

Moreover, even though the SoftMax layer can output a higher probability between background and HFs, it is not fully reliable (e.g., the probability of a pixel segmented as HF is 0.65; however, this probability is too low to identify this pixel as HF). Therefore, for decreasing the uncertainty, we set a probability threshold. Only if the probabilities of those pixels estimated to be HFs are higher than this threshold, they can be identified as clinically significant.

As displayed in Fig. 6, we gradually set the probability threshold from 0.3 to 1.0, and visualize the corresponding DSC of the test dataset. It can be observed that the best performance should be with a probability threshold = 0.9.

Comparison of Different Denoise Methods

As discussed in the previous experiment, the best patch size = 32, and the probability threshold = 0.9. On this basis, we compare the segmentation performance of the DBR network under two denoising methods.

As can be seen from Table 4, the average of precision, DSC, recall, and IOU based on the NLM filter are improved by 6.27%, 14.36%, 6.26%, and 9.43% compared to the bilateral denoise method. It demonstrates that NLM can remove speckle noise more efficiently and provide the network with more realistic, texture-informative OCT images for HF segmentation.

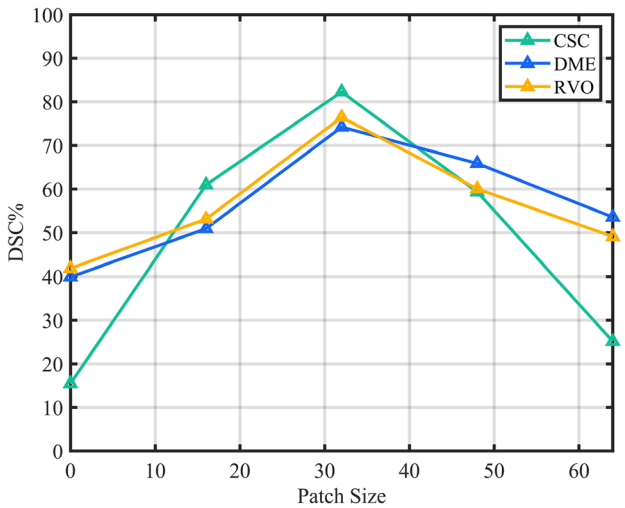

Fig. 5 Quantitative comparison of different patch sizes

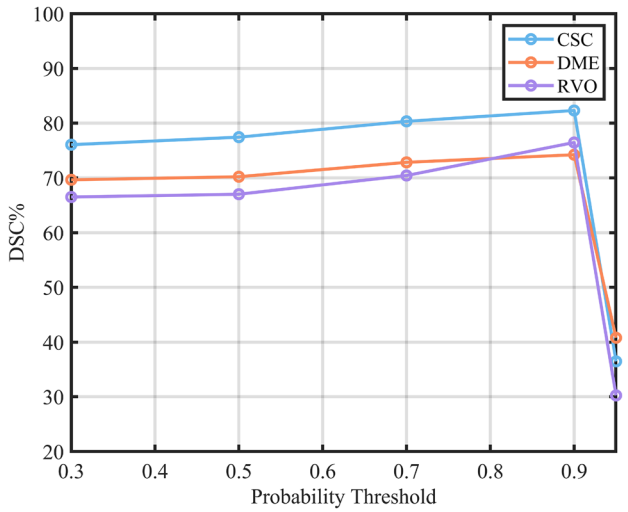

Fig. 6 Quantitative comparison of different probability threshold

Comparison of Different Segmentation Methods

With NLM filter, patch size = 32, and the probability threshold = 0.9, our proposed DBR network is compared with other state-of-the-art segmentation neural networks on three different HF segmentation tasks for fundus lesions [27–30].

Figure 7 demonstrates that our DBR network can converge faster and with a higher segmentation accuracy after 200 iterations than the other networks, thanks to the lightweight DBR parameters.

As presented in Table 5, we calculate the parameters, memory, and speed (time consumed in segmenting one OCT image) of all segmentation methods.

Note that the DBR network is able to identify the more complete HF regions and avoid wrong segmentations than other methods over all three lesion tasks as shown in Fig. 8. It indicates that the hierarchical coarse-to-fine structure of the DBR network is able to extract deep features and analyze them, resulting in the remarkable segmentation performance.

As presented in Tables 6, 7, and 8, we quantitatively analyze the evaluation metrics of precision, DSC, and recall for the mentioned methods, which proves that the performance of the DBR network is not limited by fewer parameters due to the hierarchical coarse-to-fine structure (with average DSC = 80.76% on three HF segmentation tasks, at least 5% more than others).

Discussion

HF, reflecting the inflammatory changes in OCT images, plays a crucial role in the diagnosis and treatment of fundus diseases. In this paper, we propose a lightweight approach for segmenting HF regions in OCT images, where NLM filter and patch-based image split are introduced to preprocess

Table 4 Quantitative comparison between NLM and bilateral filtering method

Disease	Precision (%)		DSC (%)		Recall (%)		IOU (%)	
	NLM	Bilateral	NLM	Bilateral	NLM	Bilateral	NLM	Bilateral
RVO	70.21 ± 2.53	68.51 ± 3.90	76.43 ± 3.06	58.62 ± 4.52	73.19 ± 3.49	70.11 ± 4.33	57.23 ± 2.78	44.38 ± 3.41
CSC	75.38 ± 3.47	73.42 ± 4.25	82.20 ± 3.75	71.35 ± 3.95	74.37 ± 3.22	69.85 ± 4.57	61.79 ± 4.23	56.52 ± 5.03
DME	81.04 ± 3.36	65.90 ± 3.78	83.65 ± 3.62	69.24 ± 4.24	80.01 ± 3.21	68.83 ± 4.98	62.08 ± 4.38	51.93 ± 4.83
Whole dataset	75.54 ± 1.37	69.27 ± 1.69	80.76 ± 1.15	66.40 ± 2.31	75.87 ± 1.92	69.60 ± 2.29	60.37 ± 1.28	50.94 ± 2.27

data. Then, a novel network consisting of DBR blocks in a hierarchical coarse-to-fine sampling architecture is used to perform HF segmentation with fewer parameters and faster inference speed. A series of experiments are conducted to evaluate the effectiveness of the proposed approach.

It was necessary to handle three aspects carefully during the segmentation of HF from the OCT images. To remove the speckle noise and retain the details of images, we propose an NLM filter to take the global information into account and yield OCT images with less noise. To solve the low proportion of HF in OCT images, patch-based image split is proposed to resize OCT images without losing any information and make the network discover more features as the proportion of HF in each patch increases. To fasten the convergence of the network and achieve greater segmentation generalization in various fundus diseases, we propose a DBR network, which is constructed with a coarse-to-fine sampling architecture. The network consists of three DBR blocks, which can leverage the dilated convolution to build multi-scale features for OCT patches with different dilated rates (from high to low), thus leading to fewer parameters and lower hardware costs.

We first compare the improvement brought by NLM and bilateral filters in HF segmentation. In the NLM filter, the target pixel is weighted by its similarity and location to all pixels in the image, while the bilateral filter just considers the set of surrounding pixels to compute the weights. Therefore, NLM makes less loss of image details and generates more pure OCT images, resulting in more effective HF segmentation.

Then, we evaluate the segmentation performance under different patch sizes and different probability thresholds. Splitting OCT images into patches can assist the neural network to focus on discovering the hidden features of HF regions in positive samples. However, the proportion of HF in a large patch size is small, and the completeness of HF in a small patch size may lose. Furthermore, setting a probability threshold can remove those HF regions of low segmentation confidence, though, the strict probability threshold may mistakenly filter out the correct segmentation results, and the loose probability threshold cannot work as mentioned above. Experiment results show that patch size = 32 and probability threshold = 0.9 can achieve the best segmentation performance.

Finally, after proving the effectiveness of the NLM filter and confirming the most suitable patch size as well as probability threshold, we compare the proposed DBR network with other state-of-the-art methods with the same preprocessing step mentioned above. The proposed network, consisting of DBR blocks, has remarkable performance in automatic segmentation of HF (83.65% of DSC in DME, 76.43% of DSC in RVO, and 82.20% of DSC in CSC), fewer parameters, and faster convergence behavior due to the fact that DBR blocks can gain wide receptive fields without the requirement of high feature resolution by performing dilated convolution operations. Moreover, the hierarchical coarse-to-fine sampling

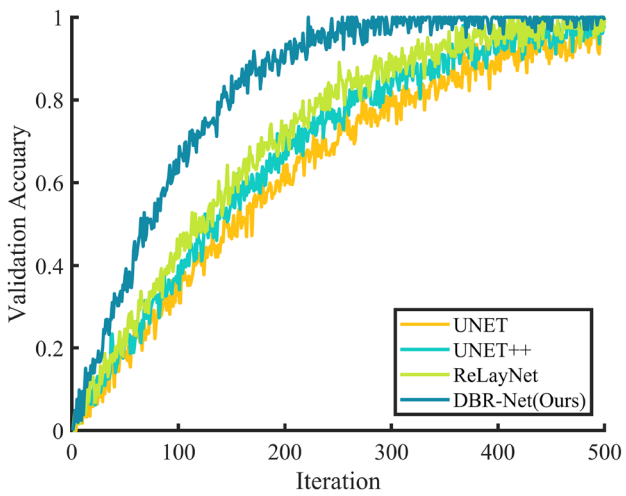

Fig. 7 Quantitative analysis of validation accuracy curves

Table 5 Model property comparison of our method and other methods

Segmentation method	Parameter (million)	Memory (million Byes)	Speed (ms/OCT image)
DBRNet (ours)	2.14	8.51	57
UNet	7.76	31.04	213
UNet++	9.04	36.17	278
RelayNet	7.08	28.39	192
FCN	12.35	48.52	447
DeeplabV3	15.11	60.47	626

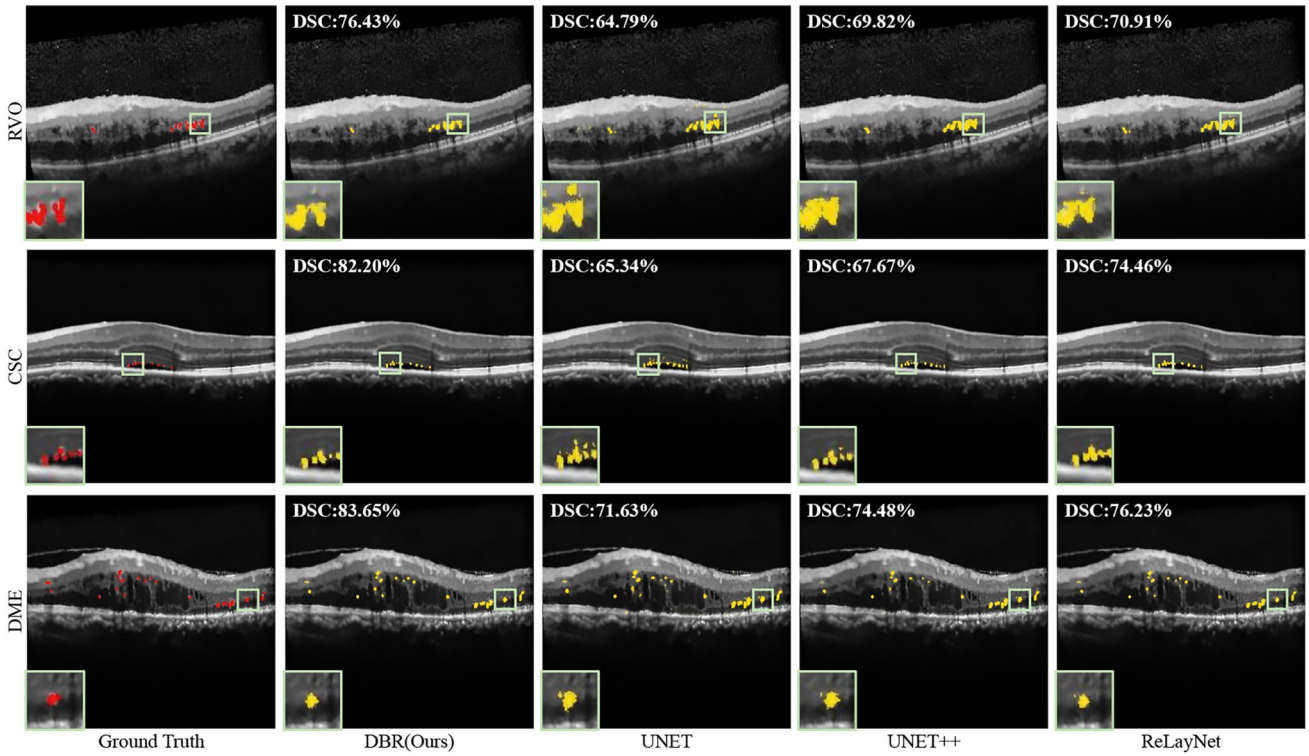

Fig. 8 Qualitative comparison of our approach and other networks

structure of the proposed DBR network can construct multi-scale features with different dilated rates, allowing it to achieve HF segmentation on a wide range of ocular diseases.

As mentioned in Table 5, the dilated rate from high to low can help DBR neural networks extract features more efficiently with fewer parameters than those composed of CNNs [33–37], which are computationally dense and time-consuming in extracting features. Therefore, under the same hardware conditions, the proposed DBR neural network requires less computing power and runs remarkably faster than other segmentation networks, showing its great potential for segmenting HF when the hardware environment cannot afford large model inference.

There were several limitations to this study. First, the participants in this study were 60.77 ± 8.77 years old, meaning the results are only applicable to this age group. Further research is needed to determine if the findings can be generalized to other age groups. Secondly, since this research was cross-sectional, our model could only detect lesions present in this database. It is unclear whether the proposed DBR network would be able to accurately segment changes in HF regions as the disease progresses, and this issue should be further investigated using external data sets.

Experiment results demonstrate the great performance of the proposed DBR network in HF segmentation, though, the datasets are mostly collected from only one hospital and the proposed DBR neural network is proven to be effective on three diseases in this paper. In the future, we will collaborate with other hospitals to obtain more datasets of different diseases and further improve the performance of the proposed DBR neural network.

Table 6 The precision of our method and other methods

	DBR (our)	UNet	UNet++	RelayNet	FCN	DeepLabv3
RVO precision (%)	70.21 ± 2.23	60.38 ± 2.43	59.86 ± 2.76	63.93 ± 2.32	57.42 ± 3.41	56.43 ± 3.56
CSC precision (%)	75.38 ± 3.47	59.53 ± 3.48	60.74 ± 3.73	72.56 ± 3.48	60.05 ± 4.17	56.79 ± 4.43
DME precision (%)	81.04 ± 3.36	61.39 ± 3.59	70.45 ± 3.92	75.83 ± 3.47	68.97 ± 4.59	66.47 ± 4.96
Whole dataset precision (%)	75.54 ± 1.37	60.43 ± 1.88	63.68 ± 1.96	70.77 ± 1.63	62.14 ± 2.20	59.89 ± 2.43

Table 7 The DSC of our method and other methods

	DBR (our)	UNet	UNet++	RelayNet	FCN	DeepLabv3
RVO DSC (%)	76.43 ± 3.06	64.79 ± 4.71	69.82 ± 4.22	70.91 ± 3.74	65.25 ± 4.67	59.54 ± 5.03
CSC DSC (%)	82.20 ± 3.75	65.34 ± 3.59	67.67 ± 3.34	74.46 ± 4.81	67.98 ± 4.32	62.83 ± 5.23
DME DSC (%)	83.65 ± 3.62	71.63 ± 4.24	74.48 ± 3.98	76.23 ± 3.52	71.01 ± 2.93	72.28 ± 4.42
Whole dataset DSC (%)	80.76 ± 1.15	67.25 ± 2.59	70.66 ± 1.76	73.87 ± 2.45	68.08 ± 1.89	64.78 ± 2.74

Table 8 The recall of our method and other methods

	DBR (our)	UNet	UNet++	RelayNet	FCN	DeepLabv3
RVO recall (%)	73.19 ± 3.49	56.42 ± 4.56	63.15 ± 3.89	64.75 ± 2.41	52.58 ± 3.32	60.32 ± 2.93
CSC recall (%)	74.37 ± 3.22	60.29 ± 4.37	63.37 ± 4.38	65.87 ± 5.28	50.16 ± 4.43	59.27 ± 3.33
DME recall (%)	80.01 ± 3.21	66.86 ± 4.23	70.92 ± 4.17	73.24 ± 4.60	59.42 ± 4.84	52.39 ± 4.89
Whole dataset recall (%)	75.87 ± 1.92	61.19 ± 2.99	65.81 ± 2.28	67.95 ± 3.42	54.05 ± 3.27	57.33 ± 3.63

Conclusion

In this paper, we present a novel method including an NLM filter, patch-based image split, and DBR block to segment accurate HF regions in OCT images. Compared with the other networks, the DBR network shows its remarkable ability to perform HF segmentation with maximum precision, DSC, and recall (at least 5% more than the other networks) as well as fast segmentation speed (57 ms/ OCT image). The proposed lightweight DBR network, suitable for HF segmentation, can provide clinically relevant information for better disease management.

Author Contribution Jin Wei, Suqin Yu, and Yupeng Xu planned the study. Yupeng Xu and Yuchen Du collected the data; Jin Wei and Suqin Yu performed statistical analyses and drafted the first version of the manuscript. Jin Wei and Yupeng Xu preprocessed the data. Yupeng Xu, Kun Liu, and Xun Xu contributed to the interpretation of the data and revised the manuscript critically for important intellectual content. All authors approved the final manuscript and agreed to be accountable for all aspects of the work.

Funding This study is supported by the National Natural Science Foundation of China (Grant No. 82201246&82171100), Medical-Engineering Funding of Shanghai Jiao Tong University (Grant No. ZH2018QNA24), and Shanghai Medical Guidance Project (Grant No.19411961800). The sponsors or funding organizations had no role in the design or conduct of this research.

Availability of Data and Materials All data included in this study are available upon reasonable request by contact with the corresponding author.

Declarations

Ethics Approval This study protocol was approved by the Institutional Review Board and Ethics Committee of Shanghai General Hospital and complied with the tenets of the Declaration of Helsinki (IRB No.: 2022SQ066).

Consent to Participate Written informed consent was obtained from individuals who participated in this study.

Consent for Publication The authors agree to publication in the Journal of Digital Imaging.

Competing Interests The authors declare no competing interests.

References

1. Romano F, Arrigo A, MacLaren RE, Charbel Issa P, Birtel J, Bandello F, Battaglia Parodi M: HYPERREFLECTIVE FOCI AS A PATHOGENETIC BIOMARKER IN CHOROIDEREMIA. Retina. 40(8):1634-1640, 2020 ;
2. Pilotto E, Miante S, Torresin T, Puthenparampil M, Frizziero L, Federle L, Gallo P, Midena E.: Hyperreflective Foci in the Retina of Active Relapse-Onset Multiple Sclerosis. Ophthalmology. 127(12):1774-1776, 2020
3. Schreur V, de Breuk A, Venhuizen FG, Sánchez CI, Tack CJ, Klevering BJ, de Jong EK, Hoyng CB: RETINAL HYPERREFLECTIVE FOCI IN TYPE 1 DIABETES MELLITUS. Retina 8:1565-1573,2020
4. Yoshitake T, Murakami T, Suzuma K, Dodo Y, Fujimoto M, Tsujikawa A: Hyperreflective Foci in the Outer Retinal Layers as a Predictor of the Functional Efficacy of Ranibizumab for Diabetic Macular Edema. Sci Rep 10(1):873, 2020
5. Kim YH, Oh J: Hyperreflective foci in the choroid of normal eyes. Graefes Arch Clin Exp Ophthalmol 3:759-769, 2022
6. Hsia Y, Yang CH, Hsieh YT, Yang CM, Ho TC, Lai TT: Hyperreflective foci in predicting the treatment outcome of antivascular endothelial growth factor in neovascular age-related macular degeneration. Graefes Arch Clin Exp Ophthalmol 2:273-280, 2020
7. Deb AK, Sarkar S. Commentary: Hyperreflective foci on optical coherence tomography and their clinical implications in diabetic macular edema. Indian J Ophthalmol 69(11):3206-3207, 2021
8. Atiskova Y, Rassuli R, Koehn AF, Golsari A, Wagenfeld L, du Moulin M, Muschol N, Dulz S: Retinal hyperreflective foci in Fabry disease. Orphanet J Rare Dis 14(1):296, 2019
9. Huang CH, Yang CH, Hsieh YT, Yang CM, Ho TC, Lai TT: Hyperreflective foci in predicting the treatment outcomes of diabetic macular

edema after anti-vascular endothelial growth factor therapy 11:5992-5103, 2021
10. Mo B, Zhou HY, Jiao X, Zhang F. Evaluation of hyperreflective foci as a prognostic factor of visual outcome in retinal vein occlusion. Int J Ophthalmol 10: 605-612, 2017
11. Hajdu D, Told R, Angeli O, Weigert G, Pollreisz A, Schmidt-Erfurth U, Sacu S. Identification of microvascular and morphological alterations in eyes with central retinal non-perfusion. PLoS One 15: 11-15, 2020
12. Qin HF, Shi FJ, Zhang CY, Luo DW, Qin SY, Wu J, Xie H, Zhang JT, Qiu QH, Liu K, Xu GT, Xu GX, Zhang JF. Anti-VEGF reduces inflammatory features in macular edema secondary to retinal vein occlusion. Int J Ophthalmol 15:1296-1304, 2022
13. Hanumunthadu D, Van Dijk EHC, Gangakhedkar S, Goud A, Cheung CMG, Cherfan D, Sarvaiya C, Banker A, Meyerle C, Boon CJ, Singh R, Wu L, Chhablani J. Gender variation in central serous chorioretinopathy. Eye (Lond) 11:1703-1709, 2018.
14. Han L, de Carvalho JRL Jr, Parmann R, Tezel TH, Chang S, Sharma T, Sparrow JR: Central Serous Chorioretinopathy Analyzed by Multimodal Imaging. Transl Vis Sci Technol 10: 9-15, 2021
15. Borrelli E, Zuccaro B, Zucchiatti I, Parravano M, Querques L, Costanzo E, Sacconi R, Prascina F, Scarinci F, Bandello F, Querques G. Optical Coherence Tomography Parameters as Predictors of Treatment Response to Eplerenone in Central Serous Chorioretinopathy. J Clin Med 8: 1265-1271, 2019
16. Mitsch C, Lammer J, Karst S, Scholda C, Pablik E, Schmidt-Erfurth UM. Systematic ultrastructural comparison of swept-source and full-depth spectral domain optical coherence tomography imaging of diabetic macular oedema. Br J Ophthalmol 7:868-873,2022
17. Grondin C, Au A, Wang D, Gunnemann F, Tran K, Hilely A, Sadda S, Sarraf D. Identification and Characterization of Epivascular Glia Using En Face Optical Coherence Tomography. Am J Ophthalmo 9:108-119, 2021
18. Lammer J, Bolz M, Baumann B: Detection and analysis of hard exudates by polarization-sensitive optical coherence tomography in patients with diabetic maculopathy,Invest Ophthalmol Vis Sci 12:1564-1571, 2014
19. Okuwobi IP, Ji Z, Fan W, Yuan S, Bekalo L, Chen Q: Automated Quantification of Hyperreflective Foci in SD-OCT With Diabetic Retinopathy. IEEE J Biomed Health Inform 24:1125-1136, 2020
20. Yu C, Xie S, Niu S, Ji Z, Fan W, Yuan S, Liu Q, Chen Q: Hyperreflective foci segmentation in SD-OCT retinal images with diabetic retinopathy using deep convolutional neural networks. Med Phys 11:4502-4519, 2019
21. Mehdizadeh M, MacNish C, Xiao D, Alonso-Caneiro D, Kugelman J, Bennamoun M. Deep feature loss to denoise OCT images using deep neural networks. J Biomed Opt 4:13-19, 2021
22. Gómez-Valverde JJ, Sinz C, Rank EA, Chen Z, Santos A, Drexler W, Ledesma-Carbayo MJ. Adaptive compounding speckle-noise-reduction filter for optical coherence tomography images. J Biomed Opt 6: 542-550, 2021
23. Zhou Q, Guo J, Ding M, Zhang X. Guided filtering-based nonlocal means despeckling of optical coherence tomography images. Opt Lett 19: 5600-5603, 2020
24. Li C, Qiu Z, Cao X, Chen Z, Gao H, Hua Z. Hybrid Dilated Convolution with Multi-Scale Residual Fusion Network for Hyperspectral Image Classification. Micromachines (Basel) 5: 522-530, 2021
25. Zhang Y, Tian Y, Kong Y, Zhong B, Fu Y. Residual Dense Network for Image Restoration. IEEE Trans Pattern Anal Mach Intell 7: 2480-2495, 2021
26. Zou K H, Warfield S K, Bharatha A, et al. Statistical validation of image segmentation quality based on a spatial overlap index1: scientific reports[J]. Academic radiology, 2004, 11(2): 178-189.
27. Xie S, Okuwobi IP, Li M, Zhang Y, Yuan S, Chen Q. Fast and Automated Hyperreflective Foci Segmentation Based on Image Enhancement and Improved 3D U-Net in SD-OCT Volumes with Diabetic Retinopathy. Transl Vis Sci Technol 4:9-21, 2020
28. Stankiewicz A, Marciniak T, Dabrowski A, Stopa M, Marciniak E, Obara B. Segmentation of Preretinal Space in Optical Coherence Tomography Images Using Deep Neural Networks. Sensors (Basel) 11:21-29, 2021
29. Song X, Xu Q, Li H, Fan Q, Zheng Y, Zhang Q, Chu C, Zhang Z, Yuan C, Ning M, Bian C, Ma K, Qu Y. Automatic quantification of retinal photoreceptor integrity to predict persistent disease activity in neovascular age-related macular degeneration using deep learning. Front Neurosci 8:16-24, 2022
30. Shen C, Liu L, Zhu L, Kang J, Wang N, Shao L. High-Throughput in situ Root Image Segmentation Based on the Improved DeepLabv3+ Method. Front Plant Sci 11. 135-147, 2021
31. Bengio Y, Grandvalet Y. No unbiased estimator of the variance of k-fold cross-validation[J]. Advances in Neural Information Processing Systems, 2003, 16.
32. Gribbon K T, Bailey D G. A novel approach to real-time bilinear interpolation[C]//Proceedings. DELTA 2004. Second IEEE international workshop on electronic design, test and applications. IEEE, 2004: 126-131.
33. Ronneberger O, Fischer P, Brox T. U-net: Convolutional networks for biomedical image segmentation[C]//International Conference on Medical image computing and computer-assisted intervention. Springer, Cham, 2015: 234–241.
34. Long J, Shelhamer E, Darrell T. Fully convolutional networks for semantic segmentation[C]//Proceedings of the IEEE conference on computer vision and pattern recognition. 2015: 3431–3440.
35. Zhou Z, Rahman Siddiquee M M, Tajbakhsh N, et al. Unet++: A nested u-net architecture for medical image segmentation[M]// Deep learning in medical image analysis and multimodal learning for clinical decision support. Springer, Cham, 2018: 3-11.
36. Roy A G, Conjeti S, Karri S P K, et al. ReLayNet: retinal layer and fluid segmentation of macular optical coherence tomography using fully convolutional networks[J]. Biomedical optics express, 2017, 8(8): 3627-3642.
37. Florian L C, Adam S H. Rethinking atrous convolution for semantic image segmentation[C]//Conference on computer vision and pattern recognition (CVPR). IEEE/CVF. 2017, 6.
38. Yao C, Wang M, Zhu W, et al. Joint Segmentation of Multi-Class Hyper-Reflective Foci in Retinal Optical Coherence Tomography Images[J]. IEEE Transactions on Biomedical Engineering, 2021, 69(4): 1349-1358.